The Variational Theory of Complex Rays for three-dimensional Helmholtz problems

Louis Kovalevsky, Pierre Ladevèze, Hervé Riou, Marc Bonnet

▶ To cite this version:

Louis Kovalevsky, Pierre Ladevèze, Hervé Riou, Marc Bonnet. The Variational Theory of Complex Rays for three-dimensional Helmholtz problems. Journal of Computational Acoustics, 2012, 20, 125021 (25 p.). 10.1142/S0218396X1250021X . hal-00714312

HAL Id: hal-00714312

https://hal.science/hal-00714312v1

Submitted on 4 Jul 2012

HAL is a multi-disciplinary open access archive for the deposit and dissemination of scientific research documents, whether they are published or not. The documents may come from teaching and research institutions in France or abroad, or from public or private research centers.

L'archive ouverte pluridisciplinaire **HAL**, est destinée au dépôt et à la diffusion de documents scientifiques de niveau recherche, publiés ou non, émanant des établissements d'enseignement et de recherche français ou étrangers, des laboratoires publics ou privés.

Journal of Computational Acoustics
© IMACS

The Variational Theory of Complex Rays for three-dimensional Helmholtz problems

Louis KOVALEVSKY
LMT Cachan,Ens Cachan/UPMC/CNRS/PRES UniverSud Paris
61 avenue du Président Wilson - 94230 Cachan, France
kovalevsky@lmt.ens-cachan.fr

Pierre LADEVÈZE
EADS Foundation Chair Advanced Computational Structural Mechanics
LMT Cachan,Ens Cachan/UPMC/CNRS/PRES UniverSud Paris
61 avenue du Président Wilson - 94230 Cachan, France
ladeveze@lmt.ens-cachan.fr

Hervé RIOU
LMT Cachan,Ens Cachan/UPMC/CNRS/PRES UniverSud Paris
61 avenue du Président Wilson - 94230 Cachan, France
riou@lmt.ens-cachan.fr

Marc BONNET
POems (UMR 7231 CNRS-ENSTA-INRIA)
32 boulevard Victor, 75015 Paris, France
marc.bonnet@ensta.fr

Received (Day Month Year)
Revised (Day Month Year)

This article proposes an extension of the Variational Theory of Complex Rays (VTCR) to three-dimensional linear acoustics, The VTCR is a Trefftz-type approach designed for mid-frequency range problems and has been previously investigated for structural dynamics and 2D acoustics. The proposed 3D formulation is based on a discretization of the amplitude portrait using spherical harmonics expansions. This choice of discretization allows to substantially reduce the numerical integration work by taking advantage of well-known analytical properties of the spherical harmonics. It also permits (like with the previous 2D Fourier version) an effective *a priori* selection method for the discretization parameter in each sub-region, and allows to estimate the directivity of the pressure field by means of a natural definition of rescaled amplitude portraits. The accuracy and performance of the proposed formulation are demonstrated on a set of numerical examples that include results on an actual case study from the automotive industry.

Keywords: Mid-frequency; Helmholtz equation; Acoustics; Variational Theory of Complex Rays; Fourier series; Spherical harmonics

1. Introduction

Numerical simulation techniques in design, analysis and optimization of systems are nowadays an essential part of the industrial design process. The standard Galerkin finite element method (FEM[1]), a well established computer aided engineering tool, is in particular commonly used for the analysis of time-harmonic dynamic problems. However, the use of continuous, piecewise-polynomial shape functions leads to very large numerical models and, in practice, restricts the application of the standard FEM to the low-frequency range. Moreover, since the shape functions are not exact solutions of the governing partial differential equations, fine discretization is required to alleviate the associated pollution error[2].

Over the recent years, a variety of techniques have been proposed to minimize these drawbacks and increase the practical range of application of the FEM to higher frequencies. Such techniques include the predefined reduced bases[3], the Galerkin least-squares FEM[4], the quasi-stabilized finite element method [5], the partition of unity method[6], the generalized finite element method[7], residual-free bubbles[8], and the quasi optimal Petrov-Galerkin method[9]. While all these methods have established abilities for reducing computational costs, their permitted frequency ranges remain below the mid- and high frequencies.

In addition to all the previously mentioned approaches, another family of solution algorithms is based on the Trefftz methods[10], which differ from FEM-type methods by expanding the unknown fields as combinations of basis functions that exactly satisfy the relevant governing partial differential equations (PDEs). Such approaches also include, for example, a special use of the partition of unity method[11], the ultra-weak variational method[12], the least-squares method[13], the discontinuous enrichment method[14], the element-free Galerkin method[15], the wave boundary element method[16] and the wave-based method[17]. The Variational Theory of Complex Rays (VTCR), which is addressed in this paper, also belongs to this family.

The main advantage of all Trefftz methods is that no refined discretization is necessary, as they use exact solutions of the governing PDE. As a result, the model size and computational effort are considerably reduced compared to element-based methods. The main differences among the various Trefftz methods lie in the treatment of the boundary conditions and the transmission conditions between sub-regions, and in the type of shape functions used.

The VTCR is based on a specially-developed weak formulation of the problem which allows the approximations in each sub-region to be *a priori* independent of one another (see[18]). Thus, in each sub-region, any type of shape function can be used provided it verifies the governing PDE. This lends great flexibility, and thus efficiency, to the approach as basis functions having clear mechanical meaning can be used without difficulty. For the acoustic vibration problems considered in this article, the VTCR approximates the solution through an integral superposition of plane waves, also known as a Herglotz wave function, ensuring exact satisfaction of the Helmholtz equation within each sub-domain. However, these functions usually violate boundary or transmission conditions. The VTCR is designed so as to enforce all boundary or transmission conditions in a weak sense, i.e. set to zero the projections of the boundary or transmission condition residuals onto the Herglotz wave functions. This process yields a matrix equation of small size, whose solution gives the angular distribution of plane waves in each sub-region. This approach has initially been proposed for mid-frequency vibrational analyses of structures, e.g. to predict the vibrational response of a 3-D plate assembly[19,20], and has later been extended to shells[21] and heterogeneous plates[22], the computation of vibrational responses[23], and transient structural dynamics[24].

More recently, the VTCR has also been considered for computing acoustic fields[25], and an adaptive version subsequently formulated[26]. Its ability to provide accurate solutions within moderate problem sizes was demonstrated through many examples. A discretization of the Herglotz wave function based on Fourier series was later proposed[27], allowing in particular to develop efficient semi-analytical techniques for the discrete VTCR problem set-up and an effective *a priori* discretization criterion. An error estimator based on dissipated energy has also been investigated[26,27].

Thus far the implementation of the linear-acoustic VTCR has been confined to 2D situations. The main goal of the present article is to propose for the first time a computationally-efficient 3D version of the linear-acoustic VTCR. The main practical difficulty faced *a priori* by 3D implementations is the potentially high numerical quadrature costs entailed by the computation of six-dimensional integrals entering the VTCR matrix entries if a fully-numerical approach is followed. This issue arises because typical integrals contributions consist of surface integrals featuring products of shape functions, each of which being defined as an integral over the unit sphere. To resolve this issue, it is proposed here to express the densities entering the Herglotz wave functions, i.e. the shape functions upon which the approximation space is built, using spherical harmonics. This is in fact the natural extension to 3D problems of the previously-developed Fourier approach for 2D acoustics. Exploitation of the analytical properties of the spherical harmonics, and in particular of their L^2-orthonormality on the unit sphere, permits analytical evaluation of all shape functions and reduce numerical quadratures from six to two dimensions. This treatment is shown here to yield an accurate and computationally efficient method, and also to permit (like with the previous 2D Fourier version) an effective *a priori* selection method for the discretization parameter in each sub-region.

This article is organized as follows. The VTCR formulation is first reviewed in Section 2. Then, the proposed 3-D version of VTCR based on a spherical harmonics decomposition of the Herglotz wave function density is presented in Section 3. A set of numerical examples designed to study the accuracy and performance of the proposed formulation, as well as results from an actual case study, are presented in Section 4. Finally, concluding remarks are given in Section 5.

2. The Variational Theory of Complex Rays for Helmholtz problems

2.1. *The reference problem*

Consider the general three-dimensional interior problem for an acoustic cavity Ω filled with a fluid characterized by its speed of sound c, its density ρ and its damping coefficient η. Assuming all excitations to be time-harmonic with a given circular frequency ω, the acoustic pressure p in Ω solves the following boundary-value problem for the Helmholtz equation:

$$\text{Find } p \in H^1(\Omega) \text{ such that } \left| \begin{array}{rll} \Delta p + k^2 p = f & \text{in } \Omega & \text{(a)} \\ p - Z L_v(p) = h_d & \text{over } \partial_Z \Omega & \text{(b)} \\ p = p_d & \text{over } \partial_p \Omega & \text{(c)} \\ L_v(p) = v_d & \text{over } \partial_v \Omega & \text{(d)} \end{array} \right. \tag{1}$$

where $k = (1 + \mathrm{i}\eta)(\omega/c) = (1 + \mathrm{i}\eta)k_0$ is the wave number, f a given source density, Z an impedance coefficient and $L_v(\Box)$ the operator expressing the normal velocity in terms of the pressure, defined by $L_v(\Box) = \mathrm{i}(\rho_0\omega)^{-1}\mathbf{n}\cdot\nabla(\Box)$, $\mathbf{n}$ being the outward normal to $\partial\Omega$. h_d, p_d and v_d denote respectively a prescribed excitation over $\partial_Z\Omega$, a prescribed pressure over $\partial_p\Omega$ and a prescribed normal velocity over $\partial_v\Omega$. The usual complex-valued representation of physical quantities is used throughout, whereby the complex amplitude $Q(\mathbf{x})$ is associated to any physical quantity of the form $\mathrm{Re}[Q(\mathbf{x})e^{-\mathrm{i}\omega t}]$ evaluated at spatial position $\mathbf{x}$ and time t (with $\mathrm{i} = \sqrt{-1}$ denoting the imaginary unit).

Let Ω be partitioned into N_Ω non-overlapping sub-cavities Ω_E ($1 \le E \le N_\Omega$), and set $\Gamma_{E,E'} = \partial\Omega_E \cap \partial\Omega_{E'}$. The reference problem (1) is then rewritten in terms of the acoustic pressure p_E in each sub-cavity Ω_E:

$$\begin{array}{l} \text{Find } (p_1, \ldots, p_{N_\Omega}) \in H^1(\Omega_1) \times \cdots \times H^1(\Omega_{N_\Omega}) \text{ such that:} \\ \left| \begin{array}{rll} \Delta p_E + k^2 p_E = f & \text{in } \Omega_E & \text{(a)} \\ p_E - Z L_v(p_E) = h_{dE} & \text{over } \partial_Z \Omega_E & \text{(b)} \\ p_E = p_{dE} & \text{over } \partial_p \Omega_E & \text{(c)} \\ L_v(p) = v_{dE} & \text{over } \partial_v \Omega_E & \text{(d)} \\ p_E = p_{E'} & \text{over } \Gamma_{EE'} & \text{(e)} \\ L_v(p_E) = -L_v(p_{E'}) & \text{over } \Gamma_{EE'} & \text{(f)} \end{array} \right. \quad (1 \le E \le N_\Omega) \end{array} \tag{2}$$

where conditions (2e,f) express the continuity conditions across $\Gamma_{E,E'}$ and p_E, Z_E, p_{dE}, h_{dE} and v_{dE} respectively denote the pressure, the impedance coefficient and the prescribed excitations for the cavity Ω_E (i.e. the restrictions of p, Z, p_d, h_d and v_E to Ω_E).

2.2. *The VTCR formulation*

The VTCR formulation is obtained from the boundary value problem (2) by rewriting it in a weak form. For this purpose, the following spaces $S^E_{ad,0}$ and S^E_{ad} of functions satisfying the homogeneous and non-homogeneous Helmholtz equation (i.e. equation (1a) with $f = 0$ or $f \neq 0$), respectively, in each sub-cavity Ω_E are introduced:

$$S^E_{ad,0} = \left\{ p_E \in H^1(\Omega_E) \quad | \quad \Delta p_E + k^2 p_E = 0 \text{ in } \Omega_E \right\}, \qquad S^E_{ad} = S^E_{ad,0} + p^p_E \tag{3}$$

where p^p_E is a particular solution of $\Delta p_E + k^2 p_E = f$ (e.g. $p^p_E(\mathbf{x}) = \int_{\Omega_E} f(\mathbf{x}) G(\mathbf{x}, \mathbf{y})\, \mathrm{d}V(\mathbf{y})$, where $G(\mathbf{x}, \mathbf{y})$ is the Green's function for the Helmholtz equation).

The VTCR formulation is:

$$\text{Find}\quad (p_1, p_2, \cdots, p_{N_\Omega}) \in S^1_{ad} \times S^E_{ad} \times \cdots \times S^{N_\Omega}_{ad} \quad \text{such that:}$$

$$\begin{aligned}
&\mathrm{Re}\Bigg\{ \frac{1}{2} \sum_{E=1}^{N_\Omega} \int_{\partial_Z \Omega_E} (p_E - Z L_v(p_E) - h_{dE})\, \overline{L_v(\delta p_E)} + \frac{1}{\bar{Z}} \overline{(p_E - Z L_v(p_E) - h_{dE})} \delta p_E \,\mathrm{d}S \\
&\qquad + \sum_{E=1}^{N_\Omega} \int_{\partial_p \Omega_E} (p_E - p_{dE})\, \overline{L_v\,(\delta p_E)}\,\mathrm{d}S + \sum_{E=1}^{N_\Omega} \int_{\cap \partial_v \Omega_E} \overline{L_v(p_E) - v_{dE}} \delta p_E \,\mathrm{d}S \\
&+ \sum_{E,E'<E} \frac{1}{2} \int_{\Gamma_{E,E'}} \Big((p_E - p_{E'})\, \overline{L_v(\delta p_E - \delta p_{E'})} + \overline{L_v(p_E + p_{E'})}.\, (\delta p_E + \delta p_{E'}) \Big)\,\mathrm{d}S \Bigg\} = 0 \\
&\qquad\qquad\qquad\qquad \forall (\delta p_1, \delta p_2, \cdots, \delta p_{N_\Omega}) \in S^1_{ad,0} \times S^2_{ad,0} \times \cdots \times S^{N_\Omega}_{ad,0}
\end{aligned} \tag{4}$$

This formulation has been shown earlier[27] to be equivalent to the reference problem (1a-d) if $\eta > 0$ or $\mathrm{Re}(Z) > 0$ (either condition corresponding to a form of damping). In the absence of dissipation, this equivalence still holds unless at frequencies that permit nonzero pressure fields satisfying the continuity conditions (2e,f) and homogeneous versions of the boundary conditions (1b–d), i.e. eigenfrequencies for the whole domain Ω subject to the latter boundary conditions.

The VTCR formulation (4) essentially consists in enforcing in a weak sense the boundary and transmission condition between subcavities. It leads to a non-symmetric linear problem. This makes the method very flexible as approximation spaces can be constructed independently for each sub-cavity, allowing the user to choose physically meaningful basis functions. Symmetric formulations for Trefftz problems are nevertheless also available[14]. They involve Lagrange multipliers, whose precise definition depends on the chosen approximation space for the pressure, resulting in larger problem sizes and increased implementation technicality. The VTCR thus emphasizes flexibility of approximation and ease of implementation over symmetry.

In practice, one sets $p_E = p^0_E + p^p_E$ in (4) and recasts it in terms of the unknowns p^0_E, with the known particular solution p^p_E contributing to the right-hand side. In the sequel, this modification will be implied throughout and attention will be focused on solving for p^0_E $(1 \le E \le N_\Omega)$ the VTCR formulation.

2.3. *Finite-dimensional approximation space*

To find approximate solutions to VCTR formulations (4), p_E is sought in each cavity Ω_E in the form $p_E = p^0_E + p^p_E$, where p^p_E is, as discussed above, a known particular solution while $p^0_E \in S^E_{ad,0}$ is taken as a *Herglotz wave function*, i.e. an integral superposition of plane waves of the form

$$\mathcal{H}[A_E](\mathbf{x}) := \int_{\mathcal{C}} A_E(\hat{\mathbf{s}}) e^{\,ik\hat{\mathbf{s}}\cdot(\mathbf{x}-\mathbf{x}_E)}\,\mathrm{d}\hat{\mathbf{s}}. \tag{5}$$

In (5), $\mathcal{C}$ is the unit sphere (or, for previous two-dimensional implementations of the VTCR, the unit circle), $\mathbf{x}_E$ is a reference point located in Ω_E and $A_E(\hat{\mathbf{s}})$ is the amplitude of the plane wave propagating in the direction $\hat{\mathbf{s}}$ that contributes to p_E. Any Herglotz wave function is a solution to the homogeneous Helmholtz equation. Moreover, it is shown elsewhere[28] that, for cavities Ω_E with smooth C^2 boundary, the space of all Herglotz wave functions with density $A_E \in L^2(\mathcal{C})$ (i.e. for which A_E is square-integrable over $\mathcal{C}$) is dense with respect to the $H^1(\Omega_E)$ norm in the space of all solutions to the Helmholtz equation. This mathematical result, which holds for any frequency[28], thus guarantees that p_E may be approximated within arbitrary accuracy by a Herglotz wave function. Keeping terminology adopted in previous work on the VCTR, the density A_E is called the *amplitude portrait* of p_E.

To achieve a discrete version of the VCTR formulation (4), finite-dimensional subspaces $S^{E,N_E}_{ad,0}$ of $S^{E}_{ad,0}$ (with N_E denoting a discretization parameter to be specified) are then constructed by discretizing the amplitude portraits A_E entering Herglotz wave functions $\mathcal{H}[A_E]$. For instance, the following approaches have been considered in previous two-dimensional implementations of the VTCR[25,27], for which $\mathcal{C}$ is the unit circle:

- $A_E(\hat{\mathbf{s}})$ is a sum of N_E Dirac distributions supported at angular locations θ_n, p_E then being the superposition of a finite number of plane waves:

  $$S^{E,N_E}_{ad,0} = \text{Span}\left\{ e^{\,ik((x-x_E).\cos\theta_n+(y-y_E).\sin\theta_n)},\ \ n=0,\ldots,N_E-1,\ \ \theta_n = \frac{2\pi n}{N_E} \right\}. \tag{6}$$

  In this case, $\text{Dim}(S^{E,N_E}_{ad,0}) = N_E$. This discretization presents the main advantage to allow analytical integration of the components of the weak formulation (4) on straight lines, but loses the continuous-superposition feature.
- $A_E(\hat{\mathbf{s}})$ is taken as piecewise-constant on $\mathcal{C}$ function, p_E then being a superposition of wave band functions:

  $$S^{E,N_E}_{ad,0} = \text{Span}\left\{ \int_{\theta_n}^{\theta_{n+1}} e^{\,ik[(x-x_E).\cos\theta+(y-y_E).\sin\theta]}\,\mathrm{d}\theta,\ \ n=0,\ldots,N_E-1,\ \ \theta_n = \frac{2\pi n}{N_E} \right\}. \tag{7}$$

  One also has $\text{Dim}(S^{E,N_E}_{ad,0}) = N_E$. This discretization retains the continuous-superposition feature, but analytical integration in (4) is not feasible even with straight lines.
- $A_E(\hat{\mathbf{s}})$ is taken as a truncated Fourier series, p_E then being a superposition of Fourier wave functions:

  $$S^{E,N_E}_{ad,0} = \text{Span}\left\{ \int_{-\pi}^{\pi} e^{\,in\theta} e^{ik((x-x_E).\cos\theta+(y-y_E).\sin\theta)}\,\mathrm{d}\theta,\ \ n=-N_E,\ldots,N_E \right\}. \tag{8}$$

  In this case, $\text{Dim}(S^{E,N_E}_{ad,0}) = 2N_E+1$. The main advantages of this discretization is that the continuous-superposition feature is preserved, while the shape functions $\mathcal{H}[A_E](\mathbf{x})$ can be evaluated analytically at any point $\mathbf{x}$. Moreover these functions make a hierarchical basis of functions, as they are nested.

The above discretizations have their pros and cons, and lead to very similar asymptotic accuracy, as seen in comparisons presented elsewhere[25,27]. For cases (6) and (7), the discretization parameter N_E, and hence $\text{Dim}(S^{E,N_E}_{ad,0})$, can be set *a priori* using a geometrical heuristic criterion: the number of shape functions must be proportional to the ratio $kR_E/(2\pi)$ of the characteristic diameter R_E of Ω_E and the wavelength (see[29], eqn. 43 or[30], eqn. 3.37). For case (8), N_E can be set *a priori* using an energetic criterion (see[27]).

3. The 3-D version of VTCR with spherical harmonics decomposition of plane waves amplitudes

The three-dimensional version of the VTCR for Helmholtz problems, which is the main focus of this article, is now developed. The discrete formulation is based on expanding the amplitude portraits over the spherical harmonics. In addition to being the natural extension to 3D problems of the previously-developed Fourier approach for 2D acoustics, this choice will be seen to permit an accurate and efficient implementation.

3.1. *Pressure field approximation*

As indicated in section 2.3, the pressure field p_E^0 in each cavity is sought as a Herglotz wave function. Introducing a parametrization of the unit sphere $\mathcal{C}$ in terms of angular spherical coordinates $(\theta,\varphi) \in [0,\pi] \times [-\pi,\pi]$, i.e. $\hat{\mathbf{s}} = \hat{\mathbf{s}}(\theta,\varphi)$ into (5), one sets:

$$p_E^0(\mathbf{x}) = \mathcal{H}[A_E](\mathbf{x}) := \int_0^\pi \left\{ \int_{-\pi}^{\pi} A_E(\theta,\varphi) e^{\,\mathrm{i}k\hat{\mathbf{s}}(\theta,\varphi)\cdot(\mathbf{x}-\mathbf{x}_E)} \,\mathrm{d}\varphi \right\} \sin\theta \,\mathrm{d}\theta, \qquad \mathbf{x} \in \Omega_E \qquad (9)$$

where $A_E(\theta,\varphi)$ is the amplitude of the plane-wave contribution to p_E^0 propagating in the $\hat{\mathbf{s}}(\theta,\varphi)$ direction.

In order to avoid a numerical quadrature over $\mathcal{C}$ (required if using e.g. ray or wave-band shape functions) and extend to the 3D case the advantages of the Fourier decomposition previously introduced[27] for 2D problems, amplitude portraits $A_E(\theta,\varphi)$ are represented as truncated Laplace series, which can be considered as the natural extension to 3D problems of the Fourier series (8). Accordingly, the discrete space $S_{ad,0}^{E,N_E}$ is now taken as:

$$\begin{aligned} S_{ad,0}^{E,N_E} &= \mathrm{Span}\Big\{ \Phi_\ell^m(\mathbf{x}), \;\; -\ell \le m \le \ell, \; 0 \le \ell \le N_E \Big\} \\ \text{with} \quad \Phi_\ell^m(\mathbf{x}) &:= \int_0^\pi \left\{ \int_{-\pi}^{\pi} Y_\ell^m(\theta,\varphi) e^{\,\mathrm{i}k\hat{\mathbf{s}}(\theta,\varphi)\cdot(\mathbf{x}-\mathbf{x}_E)} \,\mathrm{d}\varphi \right\} \sin\theta \,\mathrm{d}\theta \end{aligned} \qquad (10)$$

where $Y_\ell^m(\theta,\varphi) = Y_\ell^m(\hat{\mathbf{s}})$ denotes the spherical harmonic of (non-negative) order ℓ and index m, given by

$$\begin{aligned} Y_\ell^m(\theta,\varphi) &= \sqrt{\frac{2\ell+1}{4\pi}\frac{(l-m)!}{(l+m)!}}\, P_\ell^m(cos\theta)\, e^{\,\mathrm{i}m\varphi} \\ \text{with} \quad P_\ell^m(u) &= (-1)^m (1-u^2)^{m/2} \frac{d^m}{du^m} P_\ell(u) \quad (-\ell \le m \le \ell) \end{aligned}$$

where P_ℓ are the Legendre polynomials and P_ℓ^m are associated Legendre functions (see e.g. Secs. 8.81 and 8.91 of[31]). Amplitude portraits are thus sought in the form:

$$A_E(\theta,\varphi) = \sum_{\ell=0}^{N_E} \sum_{m=-\ell}^{\ell} a_{\ell m}^E Y_\ell^m(\theta,\varphi) \qquad (11)$$

The set $\{Y_\ell^m(\theta,\varphi)\}_{|m|\leqslant\ell\leqslant\infty}$ forms a complete orthogonal system on $\mathcal{C}$ for the $L^2(\mathcal{C})$ scalar product, denoted $(\cdot,\cdot)_{L^2(\mathcal{C})}$, and verifies

$$(Y_\ell^m, \overline{Y}_{\ell'}^{m'})_{L^2(\mathcal{C})} = \int_0^\pi \left\{ \int_{-\pi}^\pi Y_\ell^m(\theta,\varphi) \overline{Y}_{\ell'}^{m'}(\theta,\varphi)\,\mathrm{d}\varphi \right\} \sin\theta\,\mathrm{d}\theta = \delta_{\ell\ell'}\delta_{mm'}; \qquad \|Y_\ell^m\|^2_{L^2(\mathcal{C})} = 1. \quad (12)$$

Since the Y_ℓ^m are in particular linearly independent, the discrete space $S^{E,N_E}_{ad,0}$ defined by (10) has dimension $1+3+\ldots+(2N_E+1) = (N_E+1)^2$.

3.2. *Evaluation of the shape functions*

Spherical harmonics provide the natural representation of (square-integrable) amplitude portraits defined on $\mathcal{C}$. In particular, they allow analytical evaluation of the shape functions $\Phi_\ell^m(\mathbf{x})$ at any point $\mathbf{x}$ of the sub-cavity. This is achieved by invoking the Jacobi-Anger expansion[32], whereby a plane wave is written as an expansion in spherical harmonics:

$$e^{ik\hat{\mathbf{s}}\cdot\mathbf{x}} = 4\pi \sum_{\ell=0}^{+\infty} \sum_{m=-\ell}^{\ell} \mathrm{i}^\ell j_\ell(kr) Y_\ell^m(\,\hat{\mathbf{s}}\,)\overline{Y}_\ell^m(\,\hat{\mathbf{x}}\,) \quad (13)$$

where $\mathbf{x}$ is a vector with a modulus r and direction $\hat{\mathbf{x}} := \mathbf{x}/r$ and j_ℓ is the spherical Bessel function of first kind and order ℓ, linked to the Bessel function of first kind through $j_\ell(t) = \sqrt{\pi/(2t)}J_{\ell+1/2}(t)$.

Then, denoting by (r_x, θ_x, ϕ_x) the spherical coordinates associated to the relative position vector $\mathbf{x}-\mathbf{x}_E$ (i.e. setting $\mathbf{x}-\mathbf{x}_E = r_x\hat{\mathbf{x}}(\theta_x,\varphi_x)$) and using the orthonormality property (12), explicit expressions for the the shape functions $\Phi_\ell^m(\mathbf{x})$ defined by (10) are obtained:

$$\begin{aligned}
\Phi_\ell^m(\mathbf{x}) &= \int_0^\pi \left\{ \int_{-\pi}^\pi Y_\ell^m(\theta,\varphi) e^{\,\mathrm{i}k\hat{\mathbf{s}}(\theta,\varphi)\cdot(\mathbf{x}-\mathbf{x}_E)}\,\mathrm{d}\varphi \right\} \sin\theta\,\mathrm{d}\theta \\
&= \int_0^\pi \left\{ \int_{-\pi}^\pi Y_\ell^m(\theta,\varphi) \left[4\pi \sum_{\ell'=0}^{+\infty} \sum_{m'=-\ell'}^{\ell'} \mathrm{i}^{\ell'} j_{\ell'}(kr_x) Y_{\ell'}^{m'}(\theta_x,\varphi_x) \overline{Y}_{\ell'}^{m'}(\theta,\varphi) \right] \mathrm{d}\varphi \right\} \sin\theta\,\mathrm{d}\theta \\
&= 4\pi \sum_{\ell'=0}^{+\infty} \sum_{m'=-\ell'}^{\ell'} \mathrm{i}^{\ell'} j_{\ell'}(kr_x) Y_{\ell'}^{m'}(\theta_x,\varphi_x) \int_0^\pi \left\{ \int_{-\pi}^\pi Y_\ell^m(\theta,\varphi)\,\overline{Y}_{\ell'}^{m'}(\theta,\varphi)\,\mathrm{d}\varphi \right\} \sin\theta\,\mathrm{d}\theta \\
&= 4\pi \sum_{\ell'=0}^{+\infty} \sum_{m'=-\ell'}^{\ell'} \mathrm{i}^{\ell'} j_{\ell'}(kr_x) Y_{\ell'}^{m'}(\theta_x,\varphi_x)\,\delta_{\ell\ell'}\delta_{mm'} \qquad \text{(by (12))} \\
&= 4\pi\,\mathrm{i}^\ell j_\ell(kr_x) Y_\ell^m(\theta_x,\varphi_x) \qquad (14)
\end{aligned}$$

The spherical Bessel functions and spherical harmonics entering the above explicit expression of the shape functions $\Phi_\ell^m(\mathbf{x})$ can then be very efficiently evaluated numerically using low-level programming libraries. For illustration purposes, the spatial variation (14) of shape

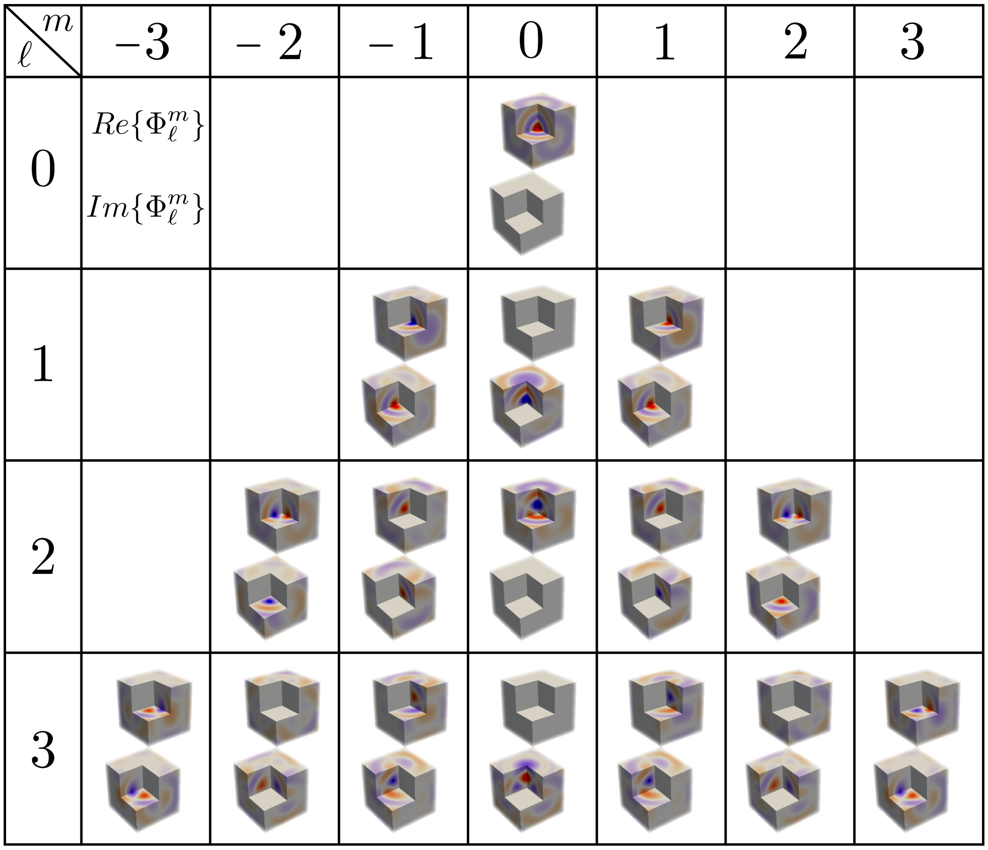

Figure 1. Real and imaginary parts of the shape functions Φ_ℓ^m given by (14), for $0 \le \ell \le 3$.

functions $\Phi_\ell^m(\mathbf{x})$ is depicted for $0 \le \ell \le 3$ in Figure 1. Then, from (9), (10), (11) and (14), the pressure field is given at any point of Ω_E by

$$p_E^0(\mathbf{x}) = \sum_{\ell=0}^{N_E} \sum_{m=-\ell}^{\ell} \Phi_\ell^m(\mathbf{x}) a_{\ell m}^E = \sum_{\ell=0}^{N_E} \sum_{m=-\ell}^{\ell} 4\pi\, \mathrm{i}^\ell j_\ell(kr_x) Y_\ell^m(\theta_x, \varphi_x) a_{\ell m}^E \qquad \mathbf{x} \in \Omega_E \tag{15}$$

Note that without the analytical result (14), one would need to perform *for each evaluation point* $\mathbf{x}$ *and each pair of indices* (ℓ, m) a numerical quadrature over $\mathcal{C}$ requiring $O(N_E^2)$ quadrature points, adding considerable computational cost to the overall discrete VTCR treatment. The computational work required for evaluating the pressure field is thus clearly proportional to the number N_{eval} of evaluation points $\mathbf{x}$.

3.3. *Discrete VTCR formulation*

Once a discretization of type (10), (11) has been chosen for each cavity, the weak formulation (4) leads to a complex-valued system of linear equations:

$$\mathbb{K}\mathbb{A} = \mathbb{F} \tag{16}$$

where the vector $\mathbb{A} = \left\{ a^E_{\ell m},\ 0 \leq \ell \leq N_E,\ -\ell \leq m \leq \ell,\ 1 \leq E \leq N_\Omega \right\}$ collects all the unknown amplitude coefficients, the influence matrix $\mathbb{K}$ corresponds to the discretization of the bilinear terms of (4) and the load vector $\mathbb{F}$ results from all linear terms of (4). The influence matrix $\mathbb{K}$ is not symmetric and may be partitioned into N^2_Ω blocks $\mathbb{K}_{EE'}$. Blocks $\mathbb{K}_{EE'}$ are zero unless the subcavities Ω_E and $\Omega_{E'}$ share a common interface $\Gamma_{EE'}$ (this includes the case $E = E'$). All nonzero blocks $\mathbb{K}_{EE'}$ are fully populated since the shape functions are defined over entire acoustic sub-cavities Ω_E. Letting N denote the total number of DOFs of the VTCR problem (i.e. the overall number of unknown coefficients $a^E_{\ell m}$), one thus has $\mathbb{K} \in \mathbb{C}^{N,N}$ and $\mathbb{A}$, $\mathbb{F} \in \mathbb{C}^N$.

To exemplify the procedure underlying the set-up of system (16), consider the computation of a typical contribution, namely that arising in (4) from a face $\partial_p\Omega_E$ of a sub-cavity Ω_E on which a prescribed pressure p_d is applied:

$$\begin{aligned}
\int_{\partial_p\Omega_E} &\left(\sum_{\ell=0}^{N_E} \sum_{m=-\ell}^{\ell} a^E_{\ell m} \Phi^m_\ell(\mathbf{x}) - p_d \right) \left(\sum_{\ell'=0}^{N_E} \sum_{m'=-\ell'}^{\ell'} \overline{\delta a^E_{\ell' m'} L_v \left(\Phi^{m'}_{\ell'}(\mathbf{x}) \right)} \right) \mathrm{d}S \\
&= \sum_{\ell'=0}^{N_E} \sum_{m'=-\ell'}^{\ell'} \overline{\delta a^E_{\ell' m'}} \left\{ \sum_{\ell=0}^{N_E} \sum_{m=-\ell}^{\ell} \left[\int_{\partial_p\Omega_E} \Phi^m_\ell(\mathbf{x}) \overline{L_v \left(\Phi^{m'}_{\ell'}(\mathbf{x}) \right)} \mathrm{d}S \right] a^E_{\ell m} \right. \\
&\qquad \left. - \int_{\partial_p\Omega_E} p_d(\mathbf{x}) \overline{L_v \left(\Phi^{m'}_{\ell'}(\mathbf{x}) \right)} \mathrm{d}S \right\}
\end{aligned} \tag{17}$$

The first and second integrals over $\partial_p\Omega_E$ in the right-hand side of (17) respectively contribute to the submatrix $\mathbb{K}_{EE}$ of the influence matrix $\mathbb{K}$ and the subvector $\mathbb{F}_E$ of the load vector $\mathbb{F}$.

As shown in section 3.2, the shape functions $\Phi^m_\ell(\mathbf{x})$ are evaluated analytically at any point $\mathbf{x}$. In expressions such as (17), the evaluation points $\mathbf{x}$ are quadrature points on relevant sub-cavity surfaces or interfaces. Moreover, the computation of $L_v \left(\Phi^m_\ell(\mathbf{x}) \right)$ is straightforward by expressing $\nabla \Phi^m_\ell$ in spherical coordinates and using the following identities:

$$\begin{aligned}
\frac{\partial}{\partial r} j_\ell(kr) &= -\frac{1}{2r} j_\ell(kr) + \frac{k}{2} j_{\ell-1}(kr) - \frac{k}{2} j_{\ell+1}(kr) \\
\frac{\partial}{\partial \theta} Y^m_\ell(\theta, \varphi) &= m \ \cot\theta \ Y^m_\ell(\theta, \varphi) + e^{-im\varphi} \sqrt{(\ell - m)(\ell + m + 1)} Y^{m+1}_\ell(\theta, \varphi) \\
\frac{\partial}{\partial \varphi} Y^m_\ell(\theta, \varphi) &= im \ Y^m_\ell(\theta, \varphi)
\end{aligned} \tag{18}$$

Then, the integrals in (17) are computed using the following approach: (i) each surface (e.g. $\partial_p\Omega_E$) is meshed (for numerical quadrature purposes only) using linear triangular C^0 elements; (ii) The Φ^m_ℓ and their derivatives are evaluated (using (14) and (18)) at the nodes; (iii) integrals are evaluated element-wise by means of usual FEM-type numerical quadrature. The quadrature mesh density must be adjusted to the acoustic wavelength. The number N_{int} of quadrature elements per wavelength is thus another important computational parameter of the VTCR. Its effect will be discussed in the numerical examples of Sec. 4. Overall, setting up the system (16) only requires numerical quadratures over surfaces, making it easy to apply the VTCR to complex geometrical configurations.

3.4. *Adjusting the discretization parameter*

In the 2D case, the energy of the Fourier shape functions (8) decays in a known way as their order $|n|$ increases[27]. This property was used to define an *a priori* selection criterion for the discretization parameter N_E in each sub-cavity Ω_E. This approach is now investigated for the 3D case, as the shape functions Φ_ℓ^m are the natural 3D generalization of the Fourier shape functions (8). The energy $e(p;\Omega)$ of a pressure field p in a domain Ω is given by

$$e(p;\Omega) := \frac{1}{\rho c^2}\int_\Omega p(\mathbf{x})\overline{p(\mathbf{x})}\,\mathrm{d}V(\mathbf{x}) \tag{19}$$

In particular, the energy of the shape function Φ_ℓ^m is estimated, from expression (14), as

$$\begin{aligned}\rho c^2 e(\Phi_\ell^m;\Omega_E) &= 16\pi^2\int_{\Omega_E}|j_\ell(kr_x)|^2|Y_\ell^m(\theta_x,\varphi_x)|^2\,\mathrm{d}V(\mathbf{x})\\ &\le 16\pi^2\int_0^{R_E}|j_\ell(kr_x)|^2 r_x^2\,\mathrm{d}r_x = \frac{2\pi^2R_E^3}{2\ell+3}\left[\frac{ekR_E}{2\ell}\right]^{2\ell}\left(1+O(\frac{1}{\ell})\right)\end{aligned} \tag{20}$$

(having invoked the orthogonality property (12)), where R_E is the radius of the smallest ball centered at $\mathbf{x}$ containing Ω_E. The last equality in (20) results from an analytical estimation of the radial integral, using the known large-order asymptotic behavior $j_\ell(z) = (2\sqrt{2}\ell)^{-1}\,[ez/2\ell]^{2\ell}(1+O\left(\ell^{-1}\right))$ of j_ℓ (see e.g. identity 10.19.1 of[33], and with $e = 2.71828\ldots$ denoting the base of the natural logarithm). The upper bound (20) shows that (i) $e(\Phi_\ell^m;\Omega_E)$ has a faster-than-exponential decay as the order ℓ becomes arbitrarily large, and (ii) that the decay sets in for values of ℓ larger than $ekR_E/2$, a threshold which is proportional to the characteristic radius of Ω_E measured in wavelengths. As an illustration, the energies $e(\Phi_\ell^m;\Omega)$ are plotted in Figure 2 for a 1m × 1m × 1m cubic cavity Ω filled with

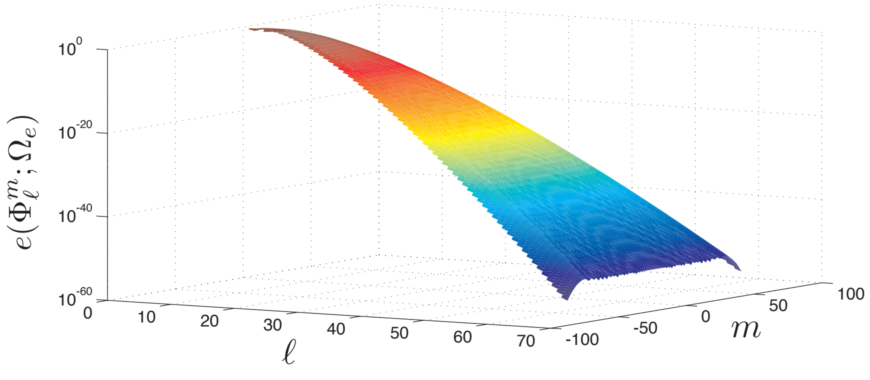

Figure 2. Energy $e(\Phi_\ell^m;\Omega_E)$ of the 3-D VTCR shape functions versus its order ℓ and momentum m.

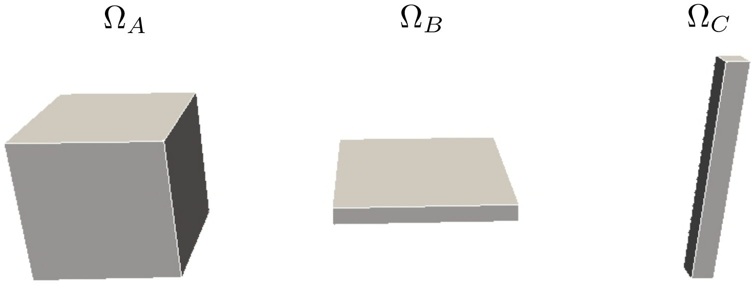

Figure 3. Convergence study (Section 3.4): geometry of box-shaped cavities Ω_A, Ω_B and Ω_C.

air at 1000 Hz. Since it is plotted using a semilog scale, the observed concave shape along the ℓ direction of the surface corroborates the predicted faster-than-exponential asymptotic decay of $e(\Phi_\ell^m;\Omega)$ with ℓ.

The largest order $\ell = N_E$ in the definition (10) of the approximation space $S_{ad,0}^{E,N_E}$ is then chosen according to

$$\forall \ell \leqslant N_E \quad \max_{|m|\leqslant \ell} \frac{e(\Phi_\ell^m;\Omega_E)}{e(\Phi_0^0;\Omega_E)} \geqslant 10^{-r} \tag{21}$$

(where r is a given number related to the desired precision). The selection criterion (21) is the direct generalization of that previously proposed[27] for 2D problems.

A sensible value for $\ell = N_E$ may alternatively be selected from a simple geometrical criterion, through

$$N_E = 2\alpha k R_E \tag{22}$$

where the desired accuracy is tuned by setting the non-dimensional coefficient α. Note that $\alpha = e/2$ corresponds to the onset of fast decay of $e(\Phi_\ell^m;\Omega_E)$ predicted by the large-order asymptotic (20).

The convergence of the VTCR is studied in the following example, where criteria (21) and (22) are compared and suitable values for parameters r and α sought. Let Ω_A, Ω_B and Ω_C be three box-shaped cavities (Figure 3) with respective dimensions $a\times a\times a$, $b\times b\times (b/10)$ and $(c/10)\times(c/10)\times c$, with the lengths a, b, c (in meters) chosen so that all eight vertices of Ω_A, Ω_B and Ω_C lie on a sphere of radius $R = 1m$. An impedance condition of type (1b) is applied over the whole cavity boundary $\partial\Omega_A$, $\partial\Omega_B$ or $\partial\Omega_C$, with $Z = 845 - 50i\text{Pa.m}^{-1}\text{.s}$. The loading $h_d(\mathbf{x})$ is defined so that the exact solution p_{ex} is

$$p_{ex}(\mathbf{x}) = \sum_{\ell=0}^{N} \sum_{m=-\ell}^{\ell} s_{\ell m} \Phi_\ell^m(\mathbf{x}) \tag{23}$$

where the maximum order N_{ex} is defined by $N_{\text{ex}} = \lfloor 20k \rfloor$, $\{s_{\ell m}\}$ is a random vector of length $(N_{\text{ex}}+1)^2$, and the reference point $\mathbf{x}_E$ entering the shape functions Φ_ℓ^m is randomly chosen inside the cavity. Five frequencies, such that $2kR =$ 10, 20, 30, 40 and 50, are considered

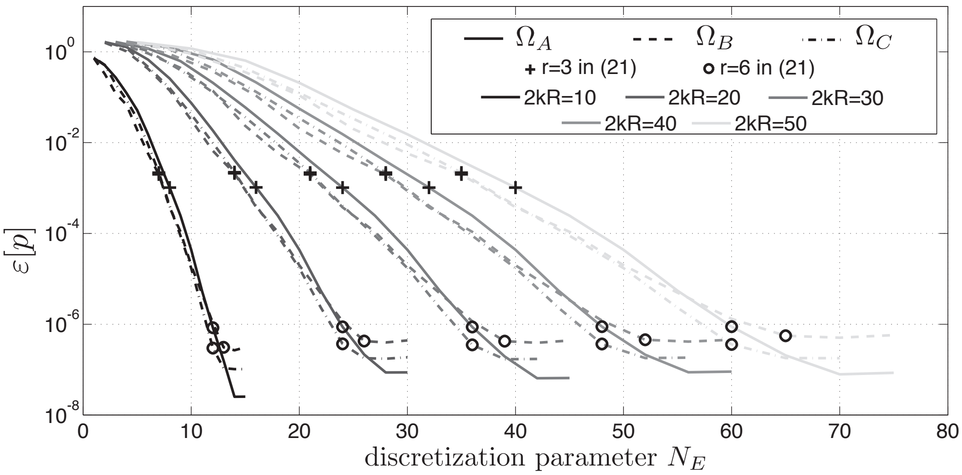

Figure 4. Convergence study (Section 3.4): Solution error $\varepsilon[p]$ (24) for the three geometries against the discretization parameter N_E, for several frequencies.

for each cavity shape. The convergence is evaluated using the relative solution error $\varepsilon[p]$:

$$\varepsilon[p] := \frac{\|p - p_{ex}\|_{H^1(\Omega)}}{\|p_{ex}\|_{H^1(\Omega)}} \tag{24}$$

Figure 4 plots the converged error (24) against N_E for cavities A, B and C. For each frequency considered, the convergence trend is similar for the three cavities. Furthermore, $\varepsilon[p] = 10^{-4}$ was found to be achieved in all cases by setting $\alpha = 1$ in (22). Indeed, $\varepsilon[p]$ is slightly lower than 10^{-4} in all cases with $N_E = 2kR$; this corresponds to setting $\alpha = 1$ in (22) (this is consistent with the previously-mentioned, somewhat larger but comparable, value $\alpha = e/2$ for the onset of rapid decrease of $e(\Phi_\ell^m, \Omega)$. In addition, Figure 4 indicates the value of N_E given by the energy-based criterion (21) with $r = 3$ (crosses) and $r = 6$ (circles). Criterion (21) is thus seen to also provide a consistent estimation of N_E for varying frequency and geometry, with achieved solution errors $\varepsilon[p]$ very similar for all the considered cases. From these results one may conclude that both criteria (21) and (22) yield good *a priori* estimates for N_E.

3.5. *Conditioning issues and rescaling of VTCR system*

The VTCR, like other numerical strategies that use oscillating functions in the approximation spaces, suffers from ill-conditioning (see for example[17,11,25]). Then, as with the 2D case[27], a preconditioner is used to reduce the effect of ill-conditioning. It is defined as the diagonal matrix $\mathbb{P} := \mathrm{Diag}\big([e(\Phi_\ell^m; \Omega_E)]^{-1/2}\big)$, and amounts to set up the VTCR system (16) using energy-normalized shape functions, i.e. to replace the representation (15) of the pressure inside a sub-cavity by

$$p_E^0(\mathbf{x}) = \sum_{\ell=0}^{N_E} \sum_{m=-\ell}^{\ell} \widehat{\Phi}_\ell^m(\mathbf{x}) \widehat{a}_{\ell m}^E \tag{25}$$

where the energy-normalized shape functions and rescaled coefficients are defined by

$$\text{(a)}\ \ \widehat{\Phi}_\ell^m(\mathbf{x}) := \left[e(\Phi_\ell^m;\Omega_E)\right]^{-1/2} \Phi_\ell^m(\mathbf{x}), \qquad \text{(b)}\ \ \widehat{a}_{\ell m}^E := \left[e(\Phi_\ell^m;\Omega_E)\right]^{1/2} a_{\ell m}^E \tag{26}$$

The scaled version $\widehat{\mathbb{K}}\,\widehat{\mathbb{A}} = \widehat{\mathbb{F}}$ of the system (16) (where $\widehat{\mathbb{K}} = \mathbb{P}\mathbb{K}\mathbb{P}$, $\widehat{\mathbb{F}} = \mathbb{P}\mathbb{F}$ and $\widehat{\mathbb{A}} = \mathbb{P}^{-1}\mathbb{A}$ is then solved using the Moore-Penrose pseudo-inverse, an approach which was found to perform satisfactorily despite the residual ill-conditioning of the rescaled matrix $\widehat{\mathbb{K}}$.

3.6. *Rescaled amplitude portrait: its interpretation and convergence*

In addition to improving the condition number of the VTCR system, the rescaled amplitude portrait defined in terms of modified coefficients (25b) is now shown to allow estimating the pressure directivity inside a sub-cavity. Indeed, using (14), the representation (25) becomes

$$p_E^0(\mathbf{x}) = \sum_{\ell=0}^{N_E} \sum_{m=-\ell}^{\ell} \phi_\ell(kr_x) Y_\ell^m(\theta_x,\varphi_x) \widehat{a}_{\ell m}^E, \tag{27}$$

with $\phi_\ell(z) := 4\pi\, \mathrm{i}^\ell \left[e(\Phi_\ell^m;\Omega_E)\right]^{-1/2} j_\ell(z)$. Now, since $\phi_\ell(kr_x)Y_\ell^m(\theta_x,\varphi_x) = \widehat{\Phi}_\ell^m(\mathbf{x})$ and due to the L^2-orthonormality of the Y_ℓ^m on $\mathcal{C}$, one has

$$\int_0^{R_E} |\phi_\ell(kr_x)|^2 r_x^2 \,\mathrm{d}r = 1$$

for any spherical sub-cavity (with R_E denoting its radius). For non-spherical sub-cavities (e.g. star-shaped sub-cavities with the upper integration bound R_E now depending on (θ_x,φ_x)), the above integral is still $O(1)$ for any ℓ. From this remark, the rescaled amplitude portrait $\widehat{A}_E$ defined by

$$\widehat{A}_E(\theta_x,\varphi_x) := \sum_{\ell=0}^{N_E} \sum_{m=-\ell}^{\ell} Y_\ell^m(\theta_x,\varphi_x) \widehat{a}_{\ell m}^E \tag{28}$$

is expected to reflect the pressure directivity inside Ω_E, and in particular to reveal the directions along which most of the energy propagates. Clearly, $\widehat{A}_E$ describes the pressure directivity more accurately than the original portrait A_E because the coefficients of the latter appear, in representation (15), as factors of non-normalized (rather than normalized) shape functions.

A directly related consideration is the fact that the convergence of p_E^0 in the $L^2(\Omega_E)$ norm as $N_E \to \infty$ does not imply the convergence of the amplitude portrait $A_E(\theta,\varphi)$ in the $L^2(\mathcal{C})$ norm. To illustrate this behavior, consider the case where $A_E(\theta,\varphi)$ is perturbed by a spurious additional term, resulting in a new distribution $\tilde{A}_E(\theta,\varphi)$ such that

$$\tilde{A}_E(\theta,\varphi) = A_E(\theta,\varphi) + \alpha Y_\ell^m(\theta,\varphi) \tag{29}$$

with α being the (finite but not necessarily small) perturbation amplitude. Let $p_E = \mathcal{H}[A_E]$ and $\tilde{p}_E = \mathcal{H}[\tilde{A}_E]$ denote the corresponding pressure fields, see (5). One then has (using orthonormality (12) of Y_ℓ^m):

$$\|A_E - \tilde{A}_E\|^2_{L^2(\mathcal{C})} = |\alpha|^2 \tag{30}$$

and hence

$$\|\widehat{A}_E - \widehat{\tilde{A}}_E\|^2_{L^2(\mathcal{C})} = |\widehat{\alpha}|^2, \tag{31}$$

where $\widehat{\alpha}$ is the rescaled perturbation amplitude given by (26b), while (see (5), (10) and (19))

$$\|p_E - \tilde{p}_E\|^2_{L^2(\Omega_E)} = |\alpha|^2 \,\|\mathcal{H}[Y_\ell^m]\|^2_{L^2(\Omega_E)} = |\alpha|^2 \,\|\Phi_\ell^m\|^2_{L^2(\Omega_E)} = |\alpha|^2 e(\Phi_\ell^m;\Omega_E) = |\widehat{\alpha}|^2. \tag{32}$$

For finite α but increasing ℓ, and due to the decay property (20) of $e(\Phi_\ell^m;\Omega_E)$, one has $\|p_E - \tilde{p}_E\|^2_{L^2(\Omega_E)} \to 0$ even though $\|A_E - \tilde{A}_E\|^2_{L^2(\mathcal{C})} \not\to 0$ as $\ell \to \infty$. In contrast, one simultaneously has $\|p_E - \tilde{p}_E\|^2_{L^2(\Omega_E)} \to 0$ and $\|\widehat{A}_E - \widehat{\tilde{A}}_E\|^2_{L^2(\mathcal{C})} \to 0$ as $\ell \to \infty$, emphasizing that the convergence on the solution p_E is correlated to that of the rescaled, rather than original, amplitude portrait. In practice, while the amplitude portrait A_E (and especially coefficients $\alpha^E_{\ell m}$ for high order n) may be sensitive to data perturbations, no stability issues arose in numerical experiments for the evaluation of p_E. Hence, unlike in some other methods such as discontinuous Galerkin formulations, no stabilization strategy (such as additional penalty terms) is implemented in the present form of the VTCR.

4. Numerical results

This section presents a set of numerical examples that were designed to study the performance of the 3D acoustic VTCR formulation (Secs. 4.1 and 4.2), followed by an actual case study (three-dimensional car cavity, Sec. 4.3). All results to follow were obtained on a MacBook with a core 2 duo 2.4Ghz CPU and a 4B RAM.

4.1. *Cubic cavity*

First, let us consider a simple cavity problem having a known exact solution. The cavity domain Ω is the cube $\big\{ (x_1, x_2, x_3) \in [0, L] \times [0, L] \times [0, L] \big\}$, and an impedance boundary condition of type (1b) is assumed over $\partial\Omega$ with Z, h_d chosen such that the exact solution p_{ex} is a plane wave propagating in the oblique spherical direction ($\theta_{ex} = 0.8, \varphi_{ex} = 2.3$). The cavity Ω is taken as a whole, i.e. is not subdivided into sub-cavities. The convergence with respect to the dimension of the approximation space $S^{E,N_E}_{ad,0}$ (see (10) and (21)) and the density N_{int} of the surface quadrature mesh (see Sec. 3.3) is evaluated for four frequencies, corresponding to $kL = 5$, 20, 35 and 50, and three quadrature densities N_{int}=7, 17 and 27. The relative solution errors $\varepsilon[p]$ (see (24)) are reported on Figure 5.

For each considered frequency, N_E (and hence the problem size $(N_E + 1)^2$) is set using criterion (21) with r varying up to 8. The 3D VTCR exhibits a very good convergence, with a rapid decrease towards very small values of the solution error as r is increased. Moreover,

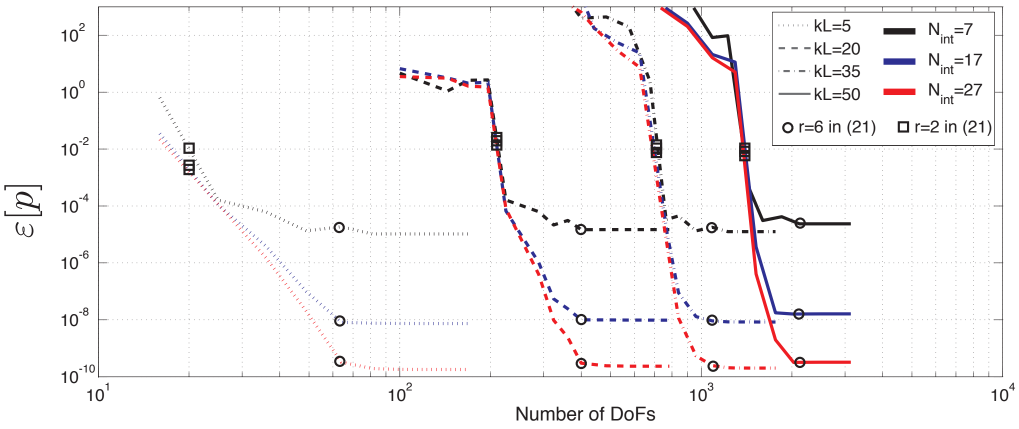

Figure 5. Cubic cavity (Section 4.1): convergence of the 3-D VTCR for the pressure field evaluation, with $kL = 5$, $kL = 20$, $kL = 35$ and $kL = 50$

.

even small values of r in criterion (21) yield an acceptable accuracy. For example, with $r = 2$ (which corresponds to the square symbol on each curve), the solution errors are already down to around 1%.

Figure 5 also shows that convergence is strongly influenced by the quadrature density N_{int}. Non-uniform convergence is seen to occur for the coarsest quadrature density N_{int}. Moreover, residual quadrature error prevents accuracy to improve beyond a certain refinement level, which depends on the chosen value of N_{int}. While high solution accuracy requires a refined surface quadrature mesh (with significant impact on the setup CPU time), one also observes that the relatively coarse quadrature density $N_{\text{int}} = 7$ is suffcient for reaching solution accuracies of the order of 1%, sufficient for many engineering applications.

The CPU times required to (i) set up the system (16), (ii) solve it, and (iii) evaluate the pressure inside the cavity using (15), respectively denoted T_{setup}, T_{solve} and T_{post}, are summarized in Table 1 for the values of kL and N_{int} considered, the problem sizes N corresponding to N_E set using $r = 6$ in (21) (the solution errors for this case being indicated

Table 1. Cubic cavity (Section 4.1): CPU times required to set up system (16), solve it, and evaluate p inside the cavity using (15)

kL	5			20			50		
N_E	64			400			2116		
N_{int}	7	17	27	7	17	27	7	17	27
T_{setup} (s)	0.18	0.36	0.78	12	62	217	332	3250	11380
T_{solve} (s)	3×10^{-4}			0.02			0.8		
N_{eval}	265			2428			39983		
T_{post} (s)	0.03			2			73		

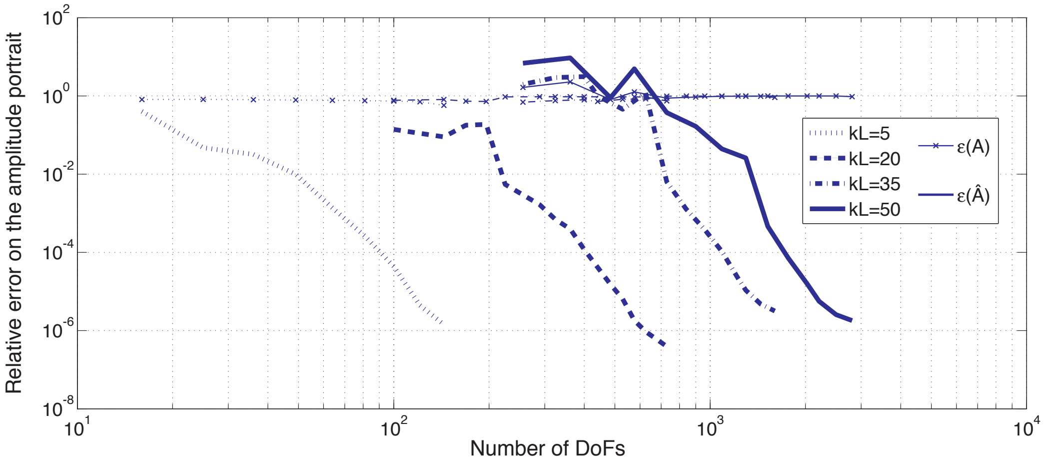

Figure 6. Cubic cavity (Section 4.1): convergence on the rescaled (bold lines) and original (fine lines) amplitude portraits.

by a circle on Figure 5). The pressure field is evaluated at N_{eval} points, the chosen values of N_{eval} corresponding to about five points per wavelength for cases $kL = 20$ and 50.

Most of the computation time is consumed in setting up system (16), a step whose cost is moreover strongly influenced, not surprisingly, by the quadrature density N_{int}. The very high value of T_{setup} observed in the $(kL, N_{\text{int}}) = (50, 27)$ case is partly due to RAM memory limitations of the computer used. The solution times are comparatively negligible, implying that the non-symmetric character of the VTCR formulation only marginally affects its overall performance.

The relative L^2 errors on both the original amplitude portrait A_E and its rescaled counterpart $\widehat{A}_E$ introduced in Sec. 3.6, denoted by $\varepsilon[A]$ and $\varepsilon[\widehat{A}]$, are reported on Figure 6. Clearly, as anticipated in Sec. 3.6, this is a situation where $\widehat{A}_E$ converges as $N_E \to \infty$ while A_E does not. Figure 7 shows the 3-D representation of the rescaled amplitude portrait for the four considered frequencies. The main direction of propagation indicated by this representation corresponds to that of the exact solution, confirming the usefulness of $\widehat{A}_E$ for physically interpreting the VTCR solution.

4.2. *Scattering by a sound-hard sphere*

The scattering of a plane wave by a sound-hard spherical obstacle, bounded by a sphere S_1 of radius $R_1 = 0.5$m, is now considered. The surrounding acoustic medium Ω is truncated by a concentric spherical surface S_2 of radius $R_2 = 1.8$m. The problem (1) is solved with the following boundary conditions: (i) $L_v(p + p_{\text{scat}}) = 0$ on S_1 (i.e. $\partial_v\Omega = S_1$) with p_{scat} denoting a plane wave propagating in the spherical direction $(\theta, \varphi) = (\pi/2, 0)$, and (ii) $p + \rho_0 c_0 L_v(p) = 0$ on S_2 (i.e. $\partial_Z\Omega = S_2$). The latter condition is an absorbing condition that approximates the Sommerfeld radiation condition. The domain Ω is decomposed into 32 sub-cavities as illustrated in Figure 8. Solution errors $\varepsilon[p]$ are evaluated with a multi-

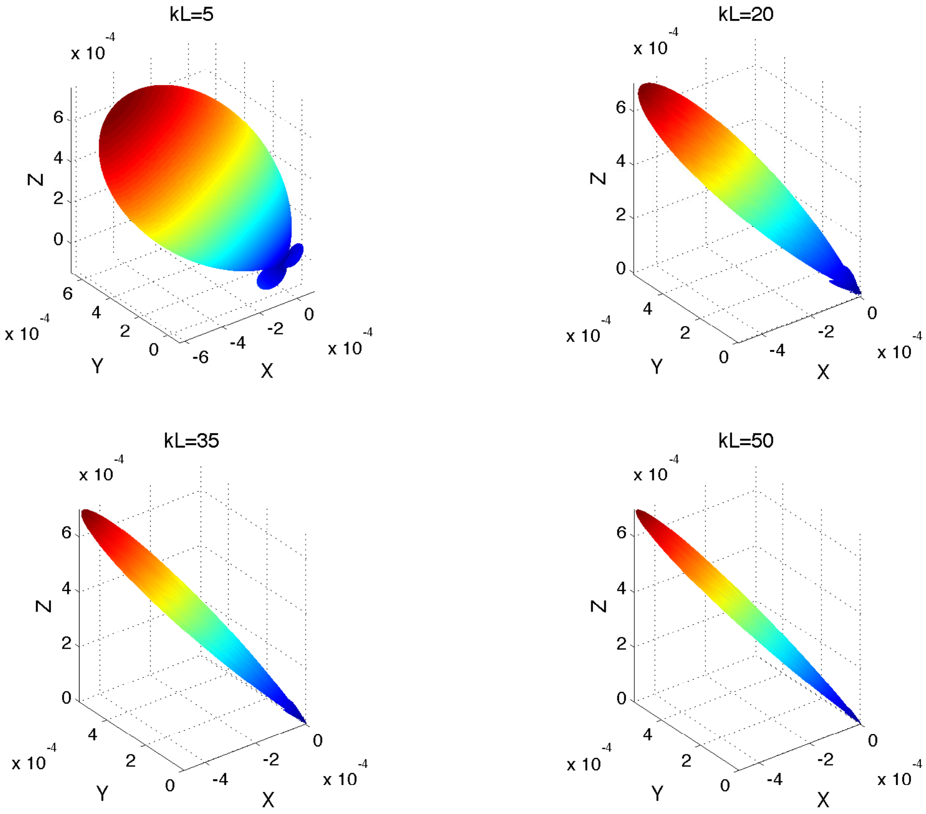

Figure 7. Cubic cavity (Section 4.1): rescaled amplitude portraits, $kL = 5$ (top left), $kL = 20$ (top right), $kL = 35$ (bottom left) and $kL = 50$ (bottom right).

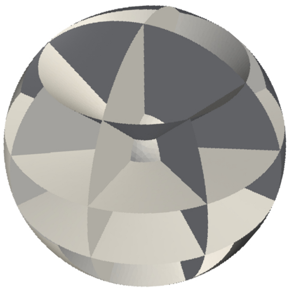

Figure 8. Scattering by a sound-hard sphere (Section 4.2): discretized computational domain.

cavity version of (24) which incorporates contributions from pressure discontinuities across interfaces $\Gamma_{EE'}$:

$$\varepsilon[p] := \frac{1}{\|p_{ex}\|_{H^1(\Omega)}} \left[\sum_{E=1}^{N_\Omega} \|p_E - p_{ex}\|^2_{H^1(\Omega_E)} + \sum_{E'<E} \|p_E - p_{E'}\|^2_{L^2(\Gamma_{EE'})} \right]^{1/2} \tag{33}$$

Using separation of variables in spherical coordinates, the exact solution of the resulting problem is known to have the analytical form

$$p^{ex}(r,\theta,\varphi) = \sum_{n=0}^{\infty} a_n(\theta,\varphi) h_n^{(1)}(kr) + b_n(\theta,\varphi) h_n^{(2)}(kr) \tag{34}$$

where $h_n^{(1)}$ and $h_n^{(2)}$ are the spherical Hankel functions of the first and second kind, respectively[33]. Coefficients $a_n(\theta,\varphi)$ and $b_n(\theta,\varphi)$ are obtained by solving the system:

$$\begin{bmatrix} h_n^{(1)\prime}(kR_1) & h_n^{(2)\prime}(kR_1) \\ h_n^{(1)\prime}(kR_2) - \mathrm{i}k h_n^{(1)}(kR_2) & h_n^{(2)\prime}(kR_2) - \mathrm{i}k h_n^{(2)}(kR_2) \end{bmatrix} \begin{Bmatrix} a_n(\theta,\varphi) \\ b_n(\theta,\varphi) \end{Bmatrix} = \begin{Bmatrix} -(2n+1)\,\mathrm{i}^n k P_n(cos\theta) j_n'(kR_1) \\ 0 \end{Bmatrix} \tag{35}$$

where j_n is the spherical Bessel function of the first kind and P_n the n^{th} Legendre polynomial. Three circular frequencies are considered, such that $2kR_1 = 5$, 20 and 35.

The real part of the scattered field is plotted in Fig. 9. The solution is consistent with physical intuition; one can for instance clearly see the reverberated and transmitted waves around the sphere.

Figure 10 reports the observed solution errors (as defined by (33)) against the total number N of DOFs. Like in Fig. 5, each error curve corresponds to a sequence of problem sizes N resulting from N_E chosen using criterion (21) with r varying from 1 to 6, with a quadrature density $N_{\text{int}} = 12$ used in all cases. Again, convergence is observed for the three considered frequencies. Convergence is however seen to be slower for the lowest frequency (for which the diameter of the sub-cavities are less than one wavelength), indicating that the VTCR indeed performs best in the mid-frequency range which motivated its design. The problem sizes yielding a relative solution error $\varepsilon[p] \approx 10^{-2}$ for the three considered

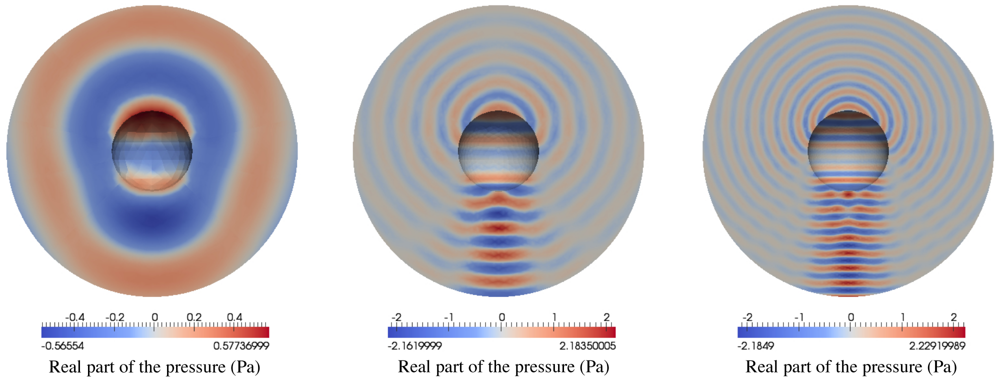

Figure 9. Scattering by a sound-hard sphere (Section 4.2): real part of the scattered pressure field for $2kR_1 = 5$ (left), $2kR_1 = 20$ (middle) and $2kR_1 = 35$(right)

.

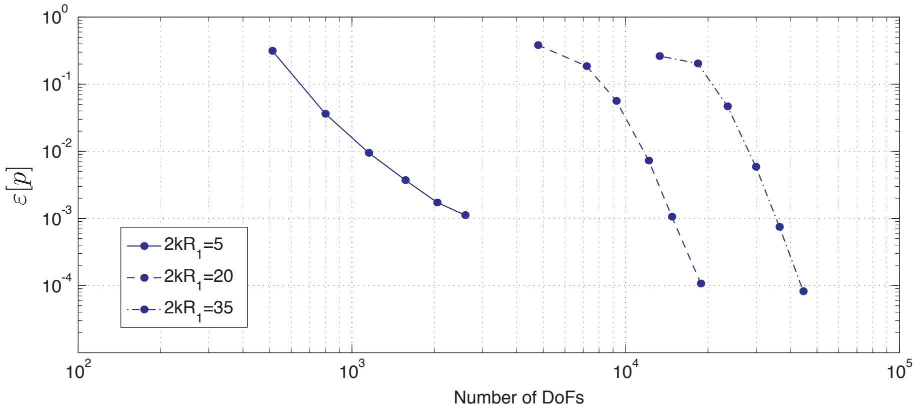

Figure 10. Scattering by a sound-hard sphere (Section 4.2): convergence curves for the relative solution error $\varepsilon[p]$ (see (33)).

frequencies are $N = 1152$, 12137 and 29902, respectively obtained with $r = 3$, 4 and 4 in (21). Note that satisfactory reconstruction errors and convergences are achieved even though this example involves non-convex sub-cavities. Using this discretization, the CPU times incurred by the VTCR (in seconds) were $(T_{\text{setup}}, T_{\text{solve}}, T_{\text{post}}) = (5.5,\ 0.1,\ 0.23)$ for $2kR_1 = 5$, $(T_{\text{setup}}, T_{\text{solve}}, T_{\text{post}}) = (719, 27, 79)$ for $2kR_1 = 20$, and $(T_{\text{setup}}, T_{\text{solve}}, T_{\text{post}}) = (4209, 353, 1189)$ for $2kR_1 = 35$ (using the notations of Table 1). Again, most of the CPU time was consumed in the setup phase, and the performance for the largest model was hindered by insufficient RAM on the used platform. A FEM mesh for the same configuration and using only seven elements per wavelength would require approximately 30500, 130900 or 689800 nodes, respectively.

Finally, Fig. 11 shows the rescaled amplitude portraits at points located on either side

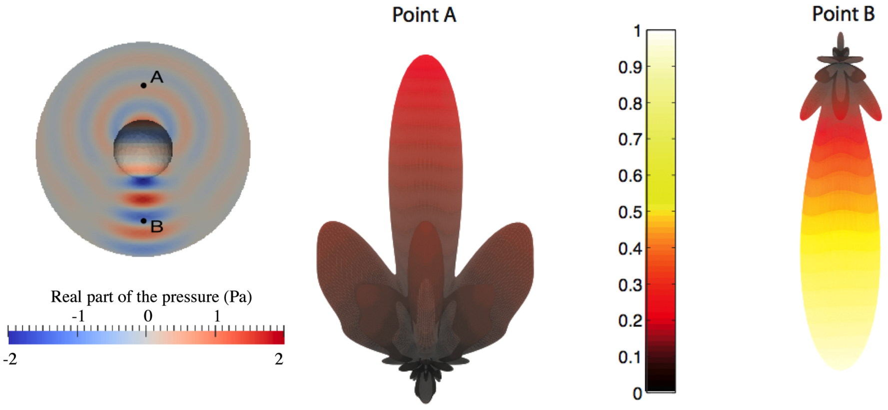

Figure 11. Scattering by a sound-hard sphere (Section 4.2): rescaled amplitude portraits computed at points A (middle) and B (right) defined in the left part

, for $2kR_1 = 12$.

of the obstacle at $2kR_1 = 12$. Again this representation correctly reveals the main direction of propagation.

4.3. *Three-dimensional car cavity*

Finally, the 3D acoustic VTCR is used to solve an acoustic problem for a car cavity (Fig. 12). The cavity, filled with air ($\rho = 1.2$ kg.m^{-3}, $c = 344$ m.s^{-1}), is excited by a point source located in the front right part of the cavity. The front and rear windows are hard walls (boundary condition of type (1d) with $v_d = 0$), while an impedance condition of type (1b) is prescribed over all other boundaries (with $Z = 845 - 55\,\mathrm{i}\ \mathrm{Pa\,s\,m^{-1}}$ on the seats and $Z = 615.4 - 1887\,\mathrm{i}\ \mathrm{Pa\,s\,m^{-1}}$ elsewhere). The cavity is decomposed into 24 sub-cavities (see the right part of Fig. 12).

The pressure field computed by the VTCR for frequencies 700, 1200 and 1700 Hz is

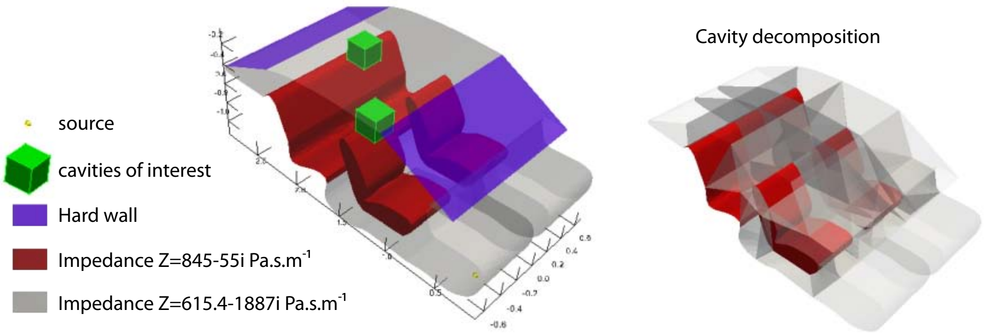

Figure 12. Definition of the car cavity of section 4.3 (boundary conditions on the left and decomposition into sub-cavities on the right).

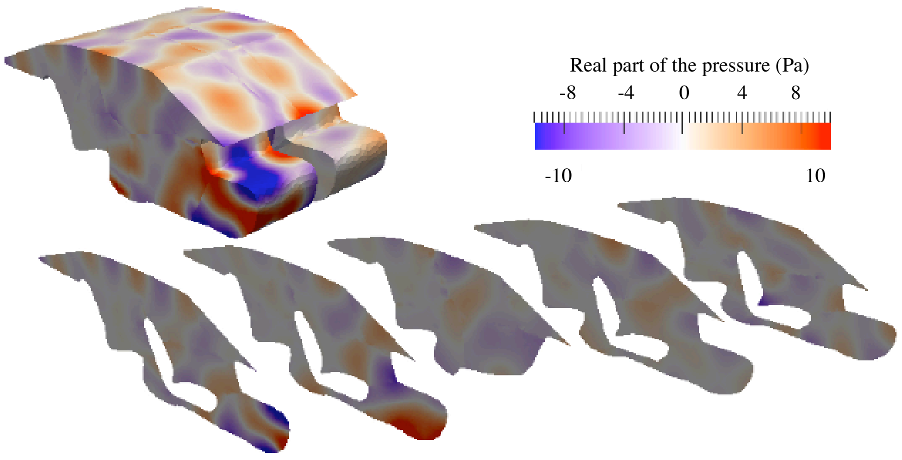

Figure 13. Real part of the pressure field computed with the 3-D VTRC in the problem defined in Figure 12 at 700 Hz.

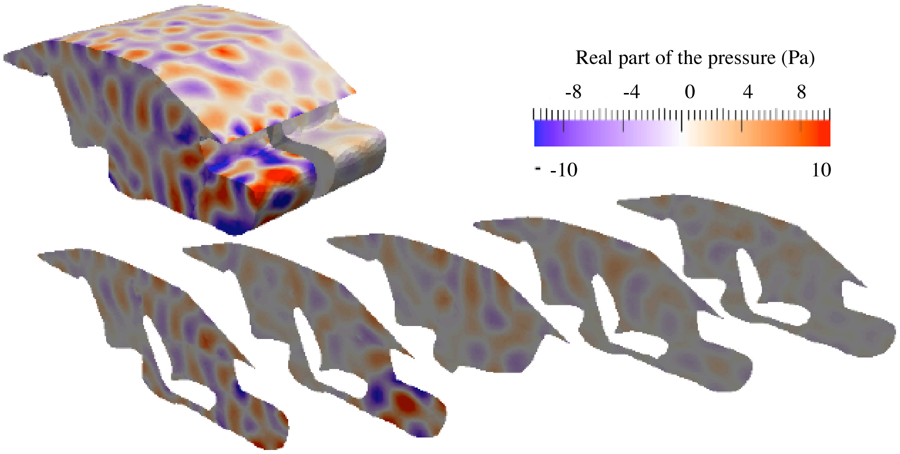

Figure 14. Real part of the pressure field computed with the 3-D VTRC in the problem defined in Figure 12 at 1200 Hz.

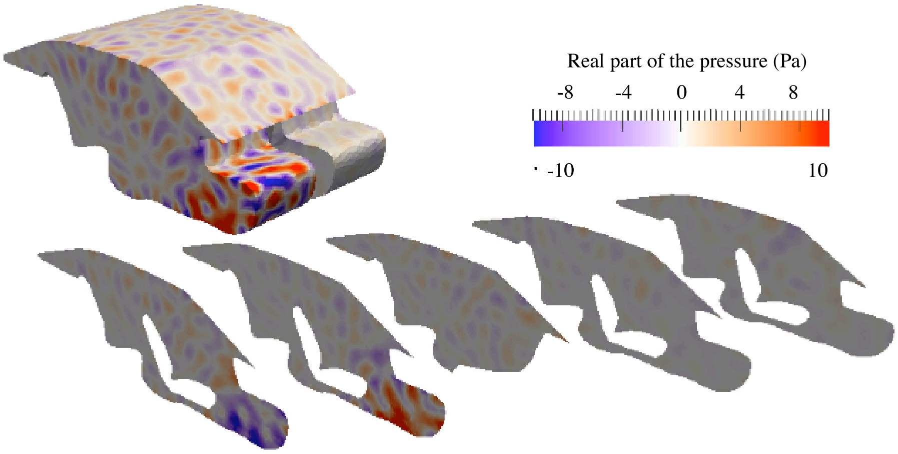

Figure 15. Real part of the pressure field computed with the 3-D VTRC in the problem defined in Figure 12 at 1700 Hz.

plotted on Figures 13, 14 and 15, respectively. Setting up and solving the system (16) required about 2 and 45 minutes of CPU time, respectively, for the 700 Hz and 1700 Hz cases, with a quadrature density $N_{\text{int}} \approx 7$. The pressure in the whole car cavity is represented by means of several planar sections. The discretization parameters N_E have been adjusted using (21) with $r = 3$, leading to $N = 4468$, 9034 and 16342 DOFs overall, respectively.

The ability of the VTCR to treat complex 3D configurations may then be exploited for evaluating quantities of industrial interest. For example, the RMS average pressure evaluated in two selected cavities of interest (shown in Fig. 12), corresponding to cubic zones of 0.2 m length where the sound ”ambiance” near the head of the front and rear passengers is

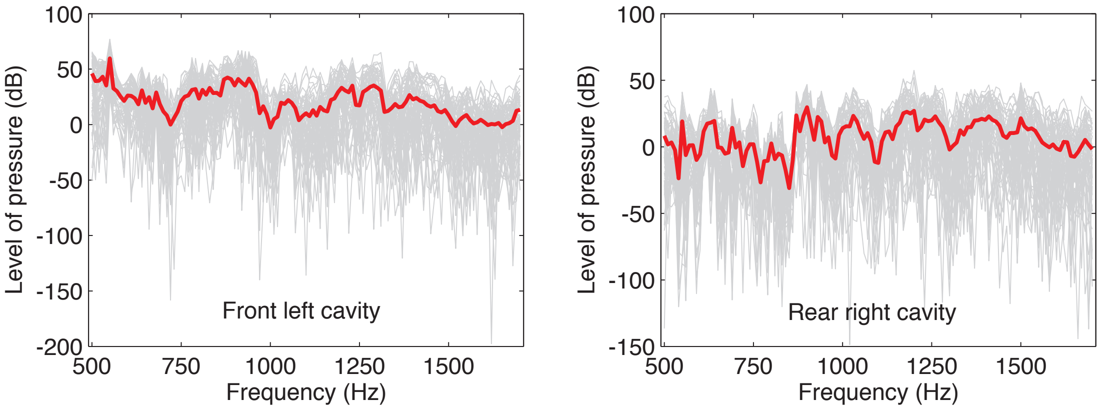

Figure 16. Evolution of the pressure of all the 64 points (grey curves) and the RMS average pressure (red bold line) inside the front left cavity (left) and rear right cavity (right) defined in Figure 12.

studied, from pressure values at 64 evenly-distributed points inside each region, and for the frequency range $[500\ \text{Hz}, 1700\ \text{Hz}]$ sampled every 10 Hz (the VTCR solution has thus been computed for each sampling frequency). The results are shown in Figure 16, where the RMS average is superposed to the pressure at all 64 evaluation points. Such information may influence the design of the car cavity.

5. Conclusion

The extension of the VTCR to 3-D acoustic problems in the medium frequency range was presented. The proposed 3-D acoustic VTCR, based on discretizing the amplitude portrait using spherical harmonics expansions, is the natural generalization of the previously-developed 2-D Fourier VTCR[27]. Various numerical experiments have been performed, demonstrating the efficiency and accuracy of the VTCR and its satisfactory convergence properties. Moreover, an estimation of the energy of the basis functions was shown to permit (like with the previous 2D Fourier version) an effective *a priori* selection method for the discretization parameter in each sub-cavity, and also to lead to a natural definition of rescaled amplitude portraits that allow to estimate the directivity of the pressure field. Future developments around this approach will include the development of a fully analytical quadrature scheme, the handling of stochastic excitations, the inclusion of approximate radiation conditions at infinity and the extension of the VTCR framework to electromagnetic waves. Future work will also address fundamental issues such as the numerical analysis of the VTCR and the study of its complexity.

Acknowledgements

The authors gratefully acknowledge the ITN Marie Curie project GA-214909 ”MID-FREQUENCY - CAE Methodologies for Mid-Frequency Analysis in Vibration and Acoustics”.

Bibliography

1. O. C. Zienkiewicz, *The Finite Element Method* (McGraw-Hill, London, 1977).
2. A. Deraemaeker, I. Babuska and P. Bouillard, Dispersion and pollution of the FEM solution for the Helmholtz equation in one, two and three dimensions, *Int. J. Numer. Meth. Eng.* **46** (1999) 471-499.
3. C. Soize. Reduced models in the medium frequency range for the general dissipative structural dynamic systems. *Eur. J. Mech. A/Solids* **17** (1998) 657-685.
4. I. Harari and T.J.R. Hughes. Galerkin/least-squares finite element methods for the reduced wave equation with non- reflecting boundary conditions in unbounded domains, *Comput. Meth. Appl. Mech. Eng.* **98** (1992) 411-454.
5. I. Babuska, F. Ihlenburg, E.T. Paik and S.A. Sauter. A generalized finite element method for solving the Helmholtz equation in two dimensions with minimal pollution, *Comput. Meth. Appl. Mech. Eng.*, **128** (1995) 325-359.
6. J.M. Melenk and I. Babuska. Approximation with harmonic and generalized harmonic polynomials in the partition of unity method. *Comput. Assist. Mech. Eng. Sci.* **4** (1997) 607-632.
7. T. Strouboulis, K. Copps and I. Babuska. The generalized finite element method: an example of its implementation and illustration of its performance, *Int. J. Numer. Meth. Eng.* **47** (2000) 1401-1417.
8. T.J.R. Hughes. Multiscale phenomena: Greens functions and the dirichlet-to-neumann formulation and subgrid scale models and bubbles and the origins of stabilized methods, *Comput. Meth. Appl. Mech. Eng.* **127** (1995) 387-401.
9. A. F. D. Loula and D. T. Fernandes. A quasi optimal Petrov-Galerkin method for Helmholtz problem, *Int. J. Numer. Meth. Eng.* **80** (2009) 1595 - 1622.
10. E. Trefftz, Ein gegenstuck zum ritzschen verfahren, in *Second International Congress on Applied Mechanics*, Zürich, Switzerland, 1926.
11. T. Strouboulis and R. Hidajat, Partition of unity method for Helmholtz equation: q-convergence for plane-wave and wave- band local bases, *Applic. Math.* **51** (2006) 181-204.
12. O. Cessenat and B. Despres, Application of an ultra weak variational formulation of elliptic PDEs to the two-dimensional Helmholtz problem, *SIAM J. Numer. Anal.* **35** (1998) 255-299.
13. P. Monk and D.Q. Wang, A least-squares method for the Helmholtz equation, *Comput. Meth. Appl. Mech. Eng.* **175** (1999) 121-136.
14. C. Farhat, I. Harari and L.P. Franca, The discontinuous enrichment method, *Comput. Meth. Appl. Mech. Eng.* **190** (2001) 6455-6479.
15. P. Bouillard and S. Suleau, Element-free Galerkin solutions for Helmholtz problems: formulation and numerical assessment of the pollution effect, *Comput. Meth. Appl. Mech. Eng.* **162** (1998) 317-335, 1998.
16. E. Perrey-Debain, J. Trevelyan and P. Bettess, Wave boundary elements: a theoretical overview presenting applications in scattering of short waves, *Eng. Anal. Bound. Elem.* **28** (2004) 131-141.
17. W. Desmet, P. Sas and D. Vandepitte, An indirect trefftz method for the steady-state dynamic analysis of coupled vibro-acoustic systems, *Comput. Assist. Mech. Eng. Sci.* **8** (2001) 271-288.
18. P. Ladevèze, A new computational approach for structure vibrations in the medium frequency range, *C.R. Acad. Sci. Paris, série II* **322** (1996) 849-856.
19. P. Ladevèze, L. Arnaud, P. Rouch and C. Blanzé, The variational theory of complex rays for the calculation of medium- frequency vibrations, *Engineering Computations* **18** (2001) 193-214.
20. R. Rouch and P. Ladevèze, The variational theory of complex rays: a predictive tool for medium-frequency vibrations, *Comput. Meth. Appl. Mech. Eng.* **192** (2003) 3301-3315.
21. H. Riou, P. Ladevèze and P. Rouch, Extension of the variational theory of complex rays to shells for medium-frequency vibrations, *J. Sound. Vibr.* **272** (2004) 341-360.

22. P. Ladevèze, L. Blanc, P. Rouch and C. Blanzé. A multiscale computational method for medium-frequency vibrations of assemblies of heterogeneous plates, *Comput. Struct.* **81** (2003) 1267-1276.
23. P. Ladevèze, P. Rouch, H. Riou and X. Bohineust, Analysis of medium-frequency vibrations in a frequency range, *J. Comput. Acoust.* **11** (2003) 255-284.
24. P. Ladevèze and M. Chevreuil, A new computational method for transient dynamics including the low- and the medium- frequency ranges, *Int. J. Numer. Meth. Eng.* **64** (2005) 503-527.
25. H. Riou, P. Ladevèze and B. Sourcis, The multiscale VTCR approach applied to acoustics problems, *J. Comput. Acoust.* **16** (2008) 487-505.
26. H. Riou, P. Ladevèze, B. Sourcis, B. Faverjon and L. Kovalevsky, An adaptive numerical strategy for the medium-frequency analysis of Helmholtz's problem, *J. Comput. Acoust.* **2** (2012).
27. L. Kovalevsky, P. Ladevèze and H. Riou, The Fourier version of the Variational Theory of Complex Rays for medium-frequency acoustics, *Comput. Meth. Appl. Mech. Eng.* **225-228** (2012) 142-153.
28. D. Colton and R. Kress, On the denseness of Herglotz wave functions and electromagnetic Herglotz pairs in Sobolev spaces, *Math. Meth. Appl. Sci.* **24** (2001) 1289-1303.
29. W. Desmet, B. van Hal, P. Sas and D. Vandepitte, A computationally efficient prediction technique for the steady-state dynamic analysis of coupled vibro-acoustic systems, *Advances Eng. Softw.* **33** (2002) 527-540.
30. B. Sourcis, Vers une stratégie adaptative de calcul pour la théorie variationnelle des rayons complexes: application à l'acoustique linéaire. PhD thesis, ENS Cachan, France (2009).
31. I. S. Gradshteyn and I. M. Ryzhik. *Tables of integrals, series and products (7th edition)*. A. Jeffreys and D. Zwillinger, editors (Elsevier, 2007).
32. D. Colton and R. Kress, *Inverse acoustic and electromagnetic scattering theory* (Springer-Verlag, 1992).
33. F.W.J. Olver, D.W. Lozier, R.F. Boisvert and C.W. Clark (editors). NIST handbook of mathematical functions (Cambridge, 2010).